Osteoblast-Induced Collagen Alignment in a 3D *in vitro* Bone Model

Judith M. Schaart[a], Mariska Kea-te Lindert[a,b], Rona Roverts[a,b], Wouter H. Nijhuis[c], Nico Sommerdijk[a,b], Anat Akiva[a,b]

[a.] Department of Medical BioSciences, Radboud University Medical Center, Geert Grooteplein Zuid 28, 6525GA Nijmegen, The Netherlands

[b.] Electron Microscopy Center, Radboudumc Technology Center Microscopy, Radboud University Medical Center, Geert Grooteplein Noord 29, 6525EZ Nijmegen, The Netherlands

[c.] Department of Orthopaedic Surgery, University Medical Centre Utrecht, Wilhelmina Children's Hospital, 3508GA Utrecht, The Netherlands

Corresponding Author: Anat Akiva

E-mail address corresponding author: anat.akiva@radboudumc.nl

Abstract

The bone extracellular matrix consists of a highly organized collagen matrix that is mineralized by hydroxyapatite. Even though the structure and composition of bone have been studied extensively, the mechanisms underlying collagen matrix organization remain elusive. In this study, we developed a 3D cell culture system in which osteogenic cells deposit an oriented collagen matrix, that is subsequently mineralized. Using live fluorescence imaging combined with volume electron microscopy, we visualize the organization of the cells and collagen in the cell culture. We show that the osteogenic cells are organizing the collagen matrix during development. Based on the observation of tunnel-like structures surrounded by aligned collagen in the center of the culture, we propose that osteoblasts organize the deposited collagen during migration towards the periphery of the culture. Overall, we show that cell-matrix interactions are involved in collagen alignment during early-stage osteogenesis and that the matrix is organized by the osteoblasts in the absence of osteoclast activity.

Keywords: Bone formation, Collagen alignment, 3D cell culture, Volume electron microscopy, 3D FIB/SEM

Abbreviations: hMSCs - human mesenchymal stem cells; FIB/SEM - Focussed Ion Beam Scanning Electron Microscopy ; AT-SEM - Array Tomography Scanning Electron Microscopy; ALP – Alkaline Phosphatase

Introduction

Bone is a highly organized tissue of which the composition and organization of the extracellular matrix, that consists mainly of collagen type 1 mineralized with calcium phosphate, are the main determinants for its mechanical properties (Fratzl and Weinkamer, 2007; Weiner and Wagner, 1998). In mature bone, both in trabecular and in cortical osteonal bone, the collagen is arranged in bundles that, in turn, form ordered arrays embedded in a disordered material (Reznikov et al., 2014). However, in most species, including humans, the first bone to be deposited during skeletal development is woven bone, where the collagen has no preferred orientation (Weiner and Wagner, 1998). Other species, such as fast-growing juvenile mammals, are born with fibrolamellar bone, a form of transient primary bone tissue in which the collagen is highly aligned in one direction (Magal et al., 2014; Weiner and Wagner, 1998). During the lifetime of the organism, the extracellular matrix is remodeled through the interplay of the different bone cell types, in which osteoclasts resorb redundant bone material, osteoblasts produce new matrix where needed, and osteocytes orchestrate this interplay. This process is also responsible for the replacement of woven and fibrolamellar bone by the cortical and trabecular lamellar bone (Katsimbri, 2017; Magal et al., 2014; Weiner and Wagner, 1998).

Already in the late 80's, Wagner and Weiner summarized the different 3D collagen organizations and their impact on the mechanical properties of the different bones, connecting structure to function (Weiner and Wagner, 1998). These models were later refined by Reznikov *et al.* (Buss et al., 2022; Reznikov et al., 2014) who used 3D focused ion beam scanning electron microscopy (3D FIB/SEM) to further elucidate the ultrastructural details of different bones. However, the mechanisms underlying the formation of these organized structures during bone formation remain largely unresolved.

In recent years, multiple 3D *in vitro* cell culture models for bone have been developed to study variable aspects of bone development (Akiva et al., 2021; Budyn et al., 2018; Nasello et al., 2020; Thrivikraman et al., 2019), which significantly improved the physiological relevance of bone cell cultures compared to previously used monolayer systems. These studies showed that mechanical stimulation (Akiva et al., 2021; Budyn et al., 2018) and matrix stiffness (Thrivikraman et al., 2019) are critical influencers of bone formation with regard to differentiation and bone matrix maturation. Remarkably, some of these 3D models showed that inducing longitudinal strain by fixation of a 3D cell culture on opposite sides was enough to induce matrix alignment and aligned mineralization (Iordachescu et al., 2018; Sasaki et al., 2010; Sasaki et al., 2015). As these models were based on only osteoblast and osteocyte-like cells, the parallel organization of the collagen cannot be attributed to a remodeling process involving osteoclasts. This suggests that such models could shed light on the mechanism of collagen orientation during fibrolamellar bone formation, which, although it occurs in many vertebrates, is still unknown.

In order to further analyze the processes underlying collagen matrix organization in the absence of osteoclastic remodeling, we developed a 3D osteogenic culture system containing a uniaxially fixed, degradable fibrin hydrogel, in which human mesenchymal stem cell (hMSC) derived osteoblasts could produce an aligned collagen matrix that was subsequently mineralized. We used this *in vitro* model to study the early-stage development of the aligned collagen matrix using fluorescence and 3D electron microscopy (volume EM). 3D FIB/SEM revealed the formation of long voids (tunnels) surrounded by layers of aligned collagen as a result of the migration of osteoblasts from the hypotrophic fibrin hydrogel core to the more nutrient-rich outer layers of the 3D culture. Formation of these "tunnels" requires a high level of control over the collagen deposition (and removal) by the osteoblasts, and we propose that a similar mechanism is likely active during fibrolamellar bone formation in many vertebrates.

Results

Establishing & Characterizing a 3D Bone Culture

A uniaxially fixed 3D cell culture was used to study cellular and collagen organization in developing bone. hMSCs were seeded as a homogeneous suspension in fibrin, supported by Velcro® strips on each side to introduce strain (Figure 1A-B). This setting facilitates cell stretching and alignment of various cell types in a 3D environment (de Jonge et al., 2013; Iordachescu et al., 2018). Two days after seeding, the culture medium was supplemented with dexamethasone and β-glycerophosphate to induce osteogenic differentiation (Jaiswal et al., 1998; Tenenbaum,

1981; Tenenbaum and Heersche, 1982). To analyze the osteogenic differentiation and architecture of the culture, 3D fluorescence microscopy and scanning electron microscopy (SEM) were combined with biochemical assays (Figure 1C-F).

The cellular distribution, collagen production, and mineral deposition were examined over the course of 28 days using live fluorescence microscopy (Figure 1C, Supplementary Figure A.1A). Evenly distributed cells and collagen, both aligned along the longitudinal direction, were present after 7 days of differentiation, indicating that, at this time, osteogenesis had already started. The first mineral signal was visible after 21 days of differentiation (Supplementary Figure A.1A), and the mineral was clearly present at day 28 (Figure 1C). During differentiation, the degradation of the fibrin scaffold was actively controlled by removing amino-caproic acid (de Jonge et al., 2013), an inhibitor of the fibrinolytic plasminogen, from the culture medium after 14 days of differentiation, after a sufficiently dense collagen matrix had been deposited by the cells. In addition, live/dead staining demonstrated the viability of the majority of the cell culture after 21 days of differentiation (Supplementary Figure A.1B).

Since the probing depth of the fluorescence imaging was limited by the high density of the cell culture (Supplementary Figure A.1C), the transversal and axial planes of the culture were imaged by SEM to visualize the composition of the bulk of the culture (Figure 1D_i-D_{ii}). These overviews showed a structure similar to the maximum intensity projections of the fluorescence imaging (Figure 1C), where the edges of the culture that interface with the Velcro® are significantly wider than the central region. This is due to the limited contraction of the gel in the region that interacts with the Velcro® anchors, which have a width of 2 to 3 mm. In combination with the thin axial cross-section of the culture (Figure 1D_{ii}), we concluded on a symmetrical radial structure of the culture. Based on the longitudinal overview, we further identified 3 distinct regions for further analysis, from the peripherical area towards the core (Figure 1D_{iii}): (i) cell-dense layer (periphery, indicated in green), (ii) collagen-rich area (bulk, indicated in magenta), and (iii) fibrin-rich area (core, indicated in blue).

In addition to these image-based analyses, biochemical assays were performed to confirm osteogenesis by quantifying calcium concentration and alkaline phosphatase (ALP) activity (Figure 1E,F). Quantification of calcium deposition in the matrix showed an overall increasing mineral content during the differentiation (Figure 1E), and this trend was retained after normalization of the calcium content to the dry weight of the demineralized cultures (Figure 1E, inset).

The cellular differentiation status in the mineralizing culture was then analyzed by quantification of ALP activity normalized to the total protein content (Figure 1F, Supplementary Figure A.1D). As expected (Husch et al., 2023; Meesuk et al., 2022; Westhauser et al., 2019), the ALP activity increased during differentiation from day 7 to day 28, after which it decreased again. The increasing ALP activity indicated that the hMSCs were maturing towards osteoblasts, as ALP expression is a marker for early osteoblast activity (Golub and Boesze-Battaglia, 2007; Zernik et al., 1990). The subsequent decrease could indicate the differentiation of osteoblasts towards more mature post-osteoblast or pre-osteocyte stages (Miron and Zhang, 2012).

Subsequently, the morphology of the cells in the fibrin-rich core of the culture was investigated by 3D array tomography SEM (AT-SEM), to analyze the cell content. This showed that most of the cells in the core of the culture have a healthy appearance despite their distance (~250-300 µm) from the nutrient-rich medium at the surface (Supplementary Figure A.1E). We inferred their healthy appearance from their size and shape and the morphology of their cellular organelles (e.g. mitochondria, nuclei, and endoplasmic reticulum). A deep-learning-based semantic segmentation algorithm was trained to automatically annotate the cells in this 3D image stack, which enabled the visualization of the 3-dimensional environment and cellular interactions. The segmentation revealed an interconnected network of cells, showing multiple protrusions and interactions (Figure 1G, Supplementary Video 1). This morphology is characteristic for osteocyte-like cells, and in line with the hypothesis that part of the osteoblasts could already have differentiated towards the final stage of osteogenesis. Overall, these data confirmed that the culture resembled crucial characteristics of bone development, including collagen production and mineralization.

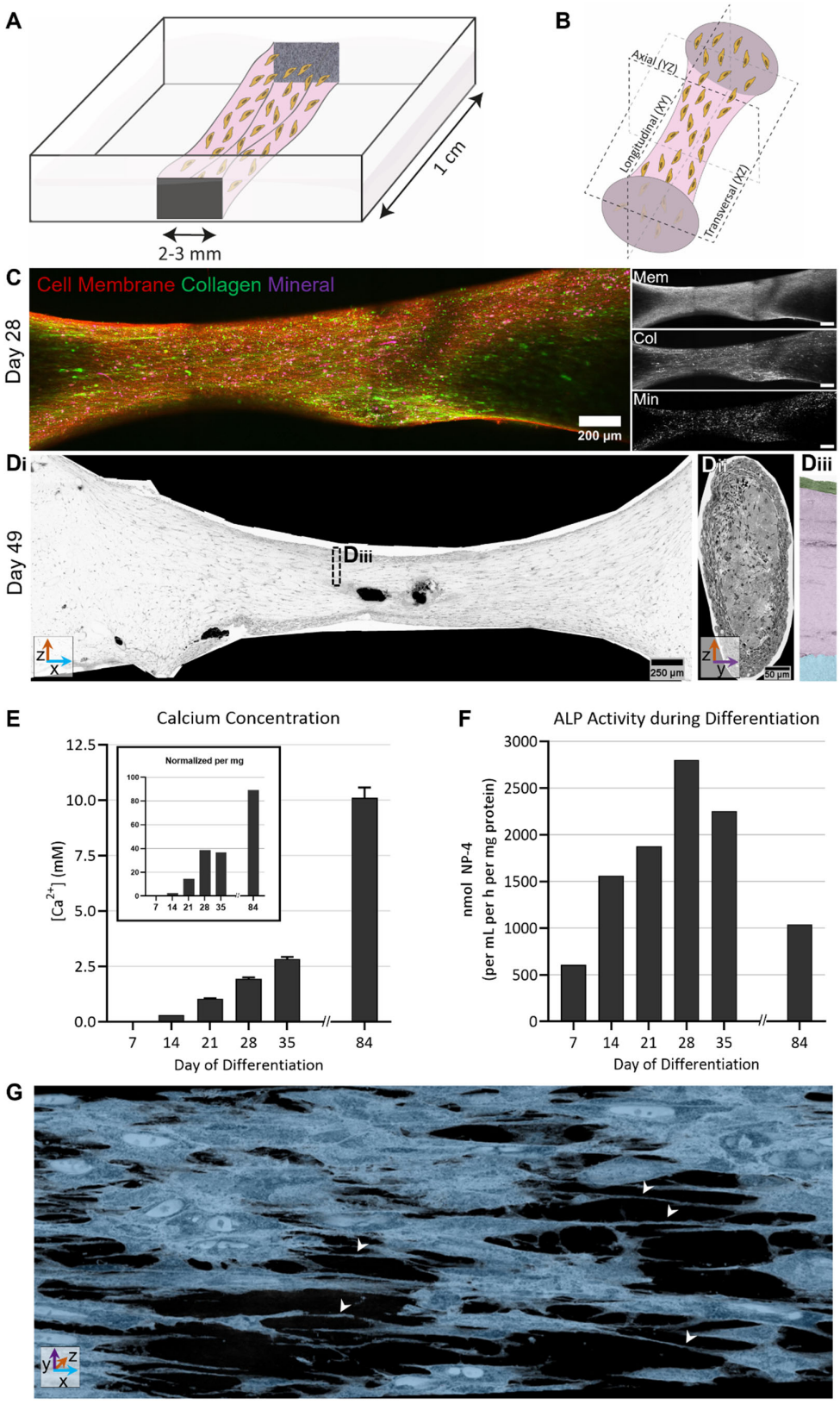

Figure 1 - Establishing a 3D osteogenic cell culture to study collagen organization

A) Schematic representation of the fibrin/cell suspension (pink) between two Velcro® fixation points (grey, 2-3mm width). The culture is grown in an Ibidi µ-slide 8-well slide, and has a length of 1 cm. B) Schematic representation of the image planes within the 3D cell culture. Transversal (XZ), longitudinal (XY) and axial (YZ) views were obtained

using 3D imaging approaches. C) The cellular distribution (Cell Mask Deep Red, red), collagen production (CNA35-OG488, green), and mineral deposition (Calcein blue, magenta) as visualized by maximum intensity projections of overview fluorescence images at 28 days of differentiation. Single channels in gray. Scale bars: 200 µm. D) SEM overview of the cross-sections of a heavy metal stained and embedded culture at day 49 of differentiation showing the outline and general organization of the osteogenic culture along the longitudinal axis (i, scale bar: 250 µm) and axial axis (ii, scale bar: 50 µm). 3 regions can be identified (iii) based on the presence of high cell density (green), mainly collagen (magenta) and fibrin (blue). E) Quantification of the deposited calcium in the matrix showed an increasing mineral content during the differentiation period. After normalization of the calcium content to the dry weight (mg) of the culture, a similar trend was observed (inset). F) Quantification of the ALP activity (normalized to the protein quantity in the sample as determined by Bradford assay, Supplementary Figure A.1D), to determine osteogenic differentiation status. G) 3D reconstruction of segmented cells from 3D AT-SEM in the fibrin-rich core of the culture. Cells show multiple protrusions (➧) and intercellular connections.

Cellular and Collagen Organization during Osteogenic Differentiation

To further analyze the cell and collagen organization during osteogenic differentiation in a dynamic approach and from an early stage of collagen production, live fluorescence microscopy was used to weekly analyze the orientation of these components in living cell cultures (Figure 2). To visualize the alignment of cells and collagen in the periphery of the culture, a color-based orientation analysis was performed on Z-stack maximum intensity projections of differentiating cultures (Figure 2A). This showed that most of the visible cells aligned along the direction of attachment (~90°) from day 7 onwards and that the cellular orientation remained stable over time. Moreover, the deposited collagen was oriented mainly in the same direction as the cells. Corresponding directionality histograms confirmed the alignment of the cells and collagen in a direction parallel to the attachment in all stages of differentiation (Figure 2B). However, overlaying the orientation histograms of the cells (Figure 2B, red) and collagen (Figure 2B, green) in the cultures at multiple differentiation time points showed that the orientation of these two components was not perfectly overlapping. When the main orientation of the collagen and the cells were compared, it was observed that the angle between these two components increased from day 4 to day 35 of differentiation (Figure 2C). After this time point, the angle between the major orientations showed a decreasing trend.

Subsequently, the alignment quality over time was analyzed by calculating the full width at half maximum (FWHM) of the directionality histograms by Lorentzian fitting (Figure 2D). Overall, the FWHM of the cell alignment (7-14°) was smaller than the FWHM of the collagen alignment (19-26°), indicating that the cells aligned more uniformly than the collagen. Furthermore, the FWHM of both components was quite stable, indicating that the alignment quality of the cells and the collagen did not change significantly during culture development. The fact that the cellular organization did not change over time indicates that the cellular morphology is stable at an osteoblast-like stage and in this time-frame does not convert during differentiation to an osteocyte-like phenotype that is expected to have more protrusions. However, the morphology of the cells observed in these fluorescence microscopy experiments only represents the cells in the periphery of the culture, as the bulk and core regions of the culture cannot be visualized due to the limited penetration depth of the live fluorescence imaging.

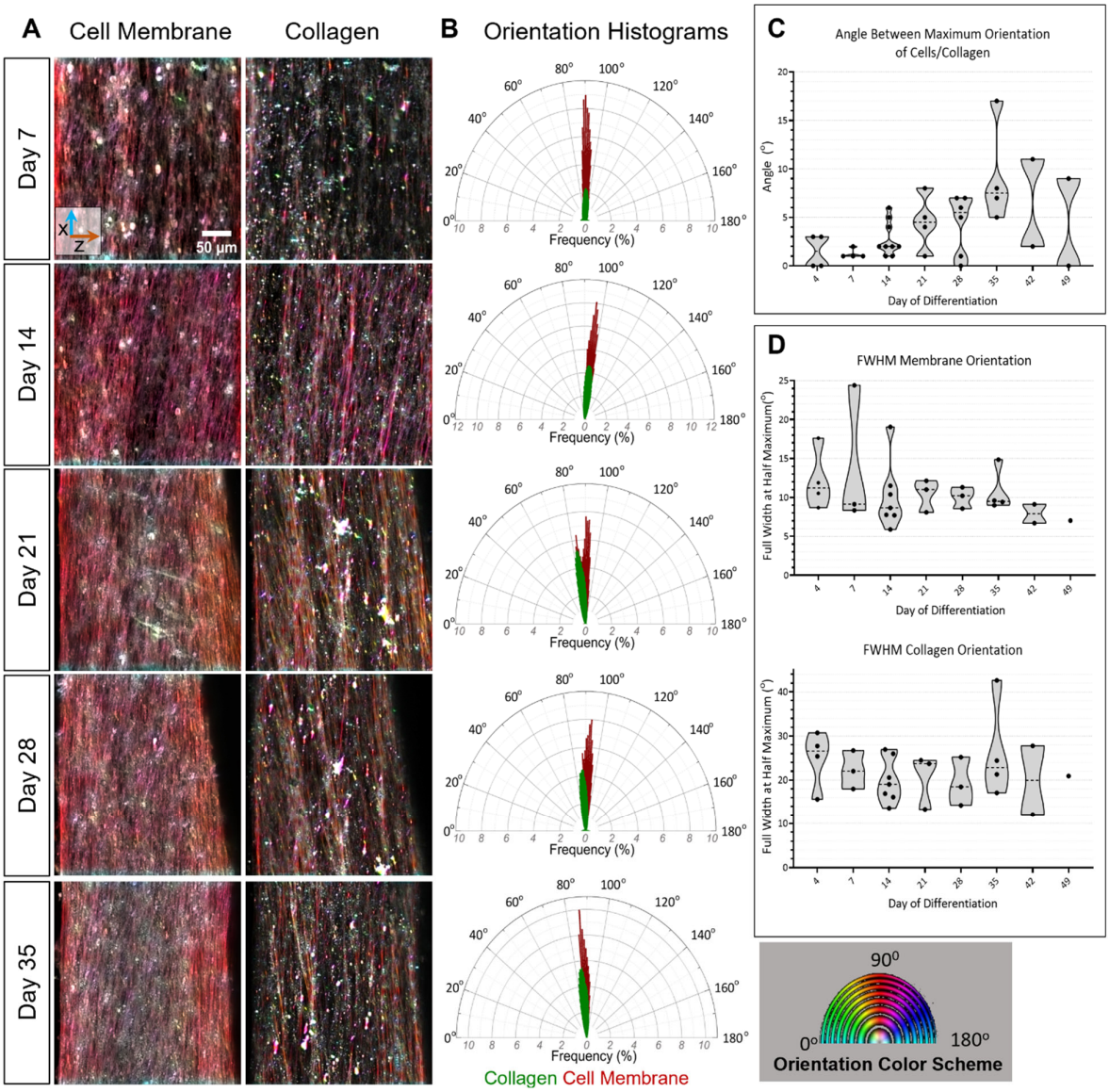

Figure 2 - Orientation of cells and collagen during differentiation

A) Color-based orientation analysis of fluorescence images (maximum intensity projections) of the cell membranes (left) and collagen matrix (right) showing that most of the visible cells aligned along the direction of the fixation. Scalebar: 50 µm. B) Orientation histograms corresponding to the fluorescence images show that the collagen deposited by the cells was oriented mainly in one direction. The plots indicated a small offset between the orientation of the cells and collagen. C) The main orientation of the collagen and the cells in multiple experiments were compared, and the angle between the two maxima was determined and plotted over time. The data indicate that the angle between these two components increased over time from day 7 to day 35 of differentiation. The angle decreased again after this time point. D) The FWHM of the directionality histograms was calculated by Lorentzian fitting and plotted for different differentiation times. The FWHM of the cell alignment was overall smaller than the FWHM of the collagen alignment during the complete culture period. The FWHM of both cellular and collagen orientation showed a slightly decreasing trend during the time of differentiation.

171 ***Cell-Collagen Interfaces in the Bulk and Core Regions***

172 To further visualize and analyze the development of the collagen and the cell-collagen interactions, 3D volume EM
173 (FIB/SEM) was performed on three regions of interest. These regions were located on the border of the cell-rich
174 periphery and collagen-rich bulk, as well as on the border between the bulk and the fibrin-rich region. Using these
175 stacks, we then further analyzed the development of the different collagen-rich regions to evaluate collagen
176 alignment, packing, and orientation in space (Figure 3, Supplementary Video 2-5). Variable densities of collagen were
177 observed, dependent on the location in the culture e.g. close to the periphery (higher density) or close to the core
178 (lower density, Supplementary Table A.1).

179 Resliced views of the transversal plane on the border of the periphery and bulk region (Figure 3A) showed that the
180 peripheral region consisted of a layer of tightly packed cells with a thickness of three to five cellular layers.
181 Surprisingly, most cells showed an elongated structure rather than a cubic one that is more phenotypic of active
182 osteoblasts (Blair et al., 2017). However, the high amount of organelles, including the mitochondrial network, that
183 the cells show suggests that these are still very active cells (Blair et al., 2017; Kassem et al., 1992). The cellular layer
184 lines a relatively thick collagen layer of about 5 µm, in which the collagen is dense and highly aligned (Figure 3A-B,
185 magenta). In this region, we can define a clear borderline between the cell-dense region and the aligned collagen
186 (Figure 3B), along which the cells stretched with rather long protrusions in the direction of the strain. In between
187 the stretched cells, the low amount of collagen showed random orientations (Figure $3B_i$), and the collagen fibers
188 seemed thinner and shorter than in the highly aligned collagen layer bordering the cell layer (Figure $3B_{ii}$). This
189 randomly organized collagen is, most likely, newly produced collagen that has not been aligned yet.

190 To visualize the relation between the cells and the collagen in the 3D volume of the highly dense collagen, deep-
191 learning-based segmentation of collagen fibrils and cells in 3D was performed on a selected region of the image
192 stack (Figure 3C-D). The 3D visualization (Figure 3F, Supplementary Video 2) showed that cells in the bulk region
193 were completely embedded in the dense, well-aligned collagen, and even though in this area the observed cell
194 density was low, the cells still aligned in the direction of the strain. Subsequently, binary images of the segmented
195 collagen were used for orientation analysis (Figure 3D-E), which confirmed the high level of alignment in this region.
196 This alignment was present in all frames throughout the complete stack (Supplementary Figure A.2A). Even in the
197 core region of the culture, where the density of the collagen was relatively low, some degree of orientation was still
198 observed (Supplementary Figure A.2B, Supplementary Video 3-4). Combining the information from the longitudinal
199 and axial image planes revealed that near the periphery the collagen directly surrounding the embedded cells closely
200 followed the outline of the cell (Figure 3C,F).

201 Interestingly, the resliced axial views of the periphery/bulk stack showed the presence of cells with elongated cell
202 protrusions towards the core of the culture and not parallel to the strain direction (Figure 3G, Supplementary Figure
203 A.3), which had morphologies typical for migrating cells, in which cellular protrusions are elongating from the cell
204 body in the direction of migration (Lu and Lu, 2021). These cells were frequently in close proximity to regions in
205 which no cellular structures or matrix were observed. From this we hypothesized that these cells were migrating
206 towards the nutrient-rich peripheral region, using these spaces to relocate their cell body, while interacting with the
207 collagen to organize and condense the matrix.

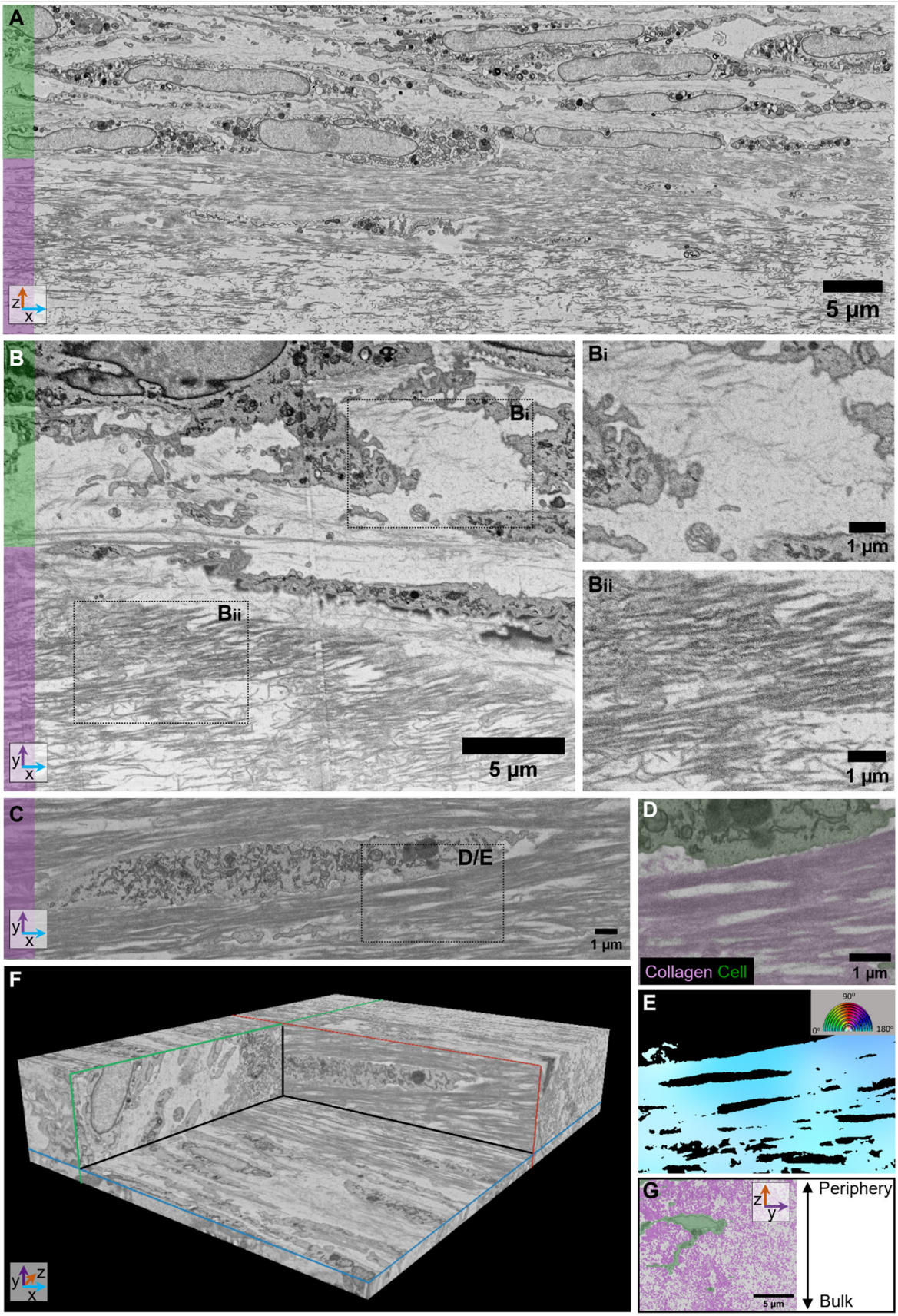
A
5 µm
B
Bi
Bii
5 µm
Bi
1 µm
Bii
1 µm
C
D/E
1 µm
D
Collagen Cell
1 µm
E
90°
0°
180°
F
G
Periphery
Bulk
5 µm

208

Figure 3 - Cell-collagen interface in the periphery and bulk region

A) Resliced transversal view from 3D FIB/SEM stack on the border of the periphery and the bulk region. The periphery region contains a high density of cells, which borders a dense region of highly aligned collagen with lower cell density in the bulk region. Scalebar: 5 µm. B) Longitudinal view from FIB/SEM imaging at the border of the periphery and the bulk region shows different collagen organizations in the different regions (scalebar: 5 µm). Collagen in the cell-dense region is observed as thin, disorganized fibers (B_i, scalebar: 1 µm), while the first layers of the bulk region consist of thicker fibers with higher density and organization (B_{ii}, scalebar: 1 µm). C) FIB/SEM image from a cell embedded in collagen in the bulk region. Scalebar: 1 µm. D) Segmented cell (green) and collagen from ROI from C. E) Color-based orientation map from collagen segmentation (ROI from C). Scalebar: 1 µm. F) Cross-sections from 3D reconstruction of FIB/SEM region, showing a cell surrounded by dense and aligned collagen. On the axial plane (YZ, green) collagen is visible as dots, while on the longitudinal (XY, red) and transversal (XZ, blue) planes the collagen is seen as threads. G) Axial view of a cell (segmented in green) with a body and tail, proposedly migrating through the collagen from the bulk towards the periphery region. Scalebar: 5 µm.

Cell-Shaped Tunnels and Voids in the Collagen Matrix

Next, the collagen organization and cell-collagen interfaces in the FIB/SEM stack recorded around the bulk/fibrin border were analyzed (Figure 4). Overall, the collagen density in this region was lower than close to the periphery (Supplementary Table A.1). However, more condensed regions of well-aligned collagen were observed in close proximity to cells (Figure 4A-C), and cells still show a preferred orientation along the longitudinal axis of the culture. In addition to the cells embedded in denser and well-aligned collagen, cell-free regions surrounded by organized collagen extending from cell protrusions were also observed (Figure 4A, *). Interestingly, although cells are not detected in these regions, these collagen fibrils border voids that could fit cell protrusions. After automated segmentation of cells and collagen, the 3D reconstruction of the cell protrusions and the proximate collagen showed that these cell-shaped voids form tunnels, outlined by collagen walls (Figure 4B, collagen: magenta, cell: green, Supplementary Video 5), which is also confirmed by visualization of the axial view of these voids (Figure 4B_i).

When comparing the collagen density around these tunnels (Figure 4A-B_i) to the collagen density around a cell body (Figure 4C) it was observed that highly aligned collagen is present both around the cells (Figure 4C) and the voids (Figure 4A). Additionally, the axial cross-sections show a gradient in the collagen density surrounding the cells and the voids, with a pattern of more densely packed and better-organized collagen closer to the cells (Figure 4B_i) and voids (Figure 4C_{ii}). We therefore propose that these cell-free tunnels are created by the retraction of the cell after depositing the aligned collagen layer.

Similar observations regarding collagen organization and density were made for regions with collagen surrounded cell-shaped voids (Figure 4D). Even though no neighboring cell was observed in the reconstructed volume, the cell-like shape remained as a hole in the aligned collagen matrix (Figure 4E).

When analyzing the fibrin-rich core of the culture, 3D AT-SEM showed that cells still have a preferred alignment along the longitudinal axis of the culture (Figure 4F). Interestingly, also the fibrin-embedded cells were regularly surrounded by regions in which no cellular structures or protein matrix were observed in the 3D AT-SEM volume, and the tunnels seemed to form connections between different cells (Figure 4F, orange, Supplementary Figure A.2C). Looking at these data in more detail showed that the observed tunnels were more tight in regions with a mixed fibrin-collagen matrix (Supplementary Figure A.2D, *), while the voids of cells surrounded by pure fibrin were wider and less structured (Supplementary Figure A.2D, ▼). This could possibly be due to higher stability induced by crosslinking of the *collagen* matrix, as well as degradation of the *fibrin* matrix by the cells. Overall, these observations indicated that the extracellular matrix in these cultures was organized during osteogenic differentiation by osteogenic cells in the culture.

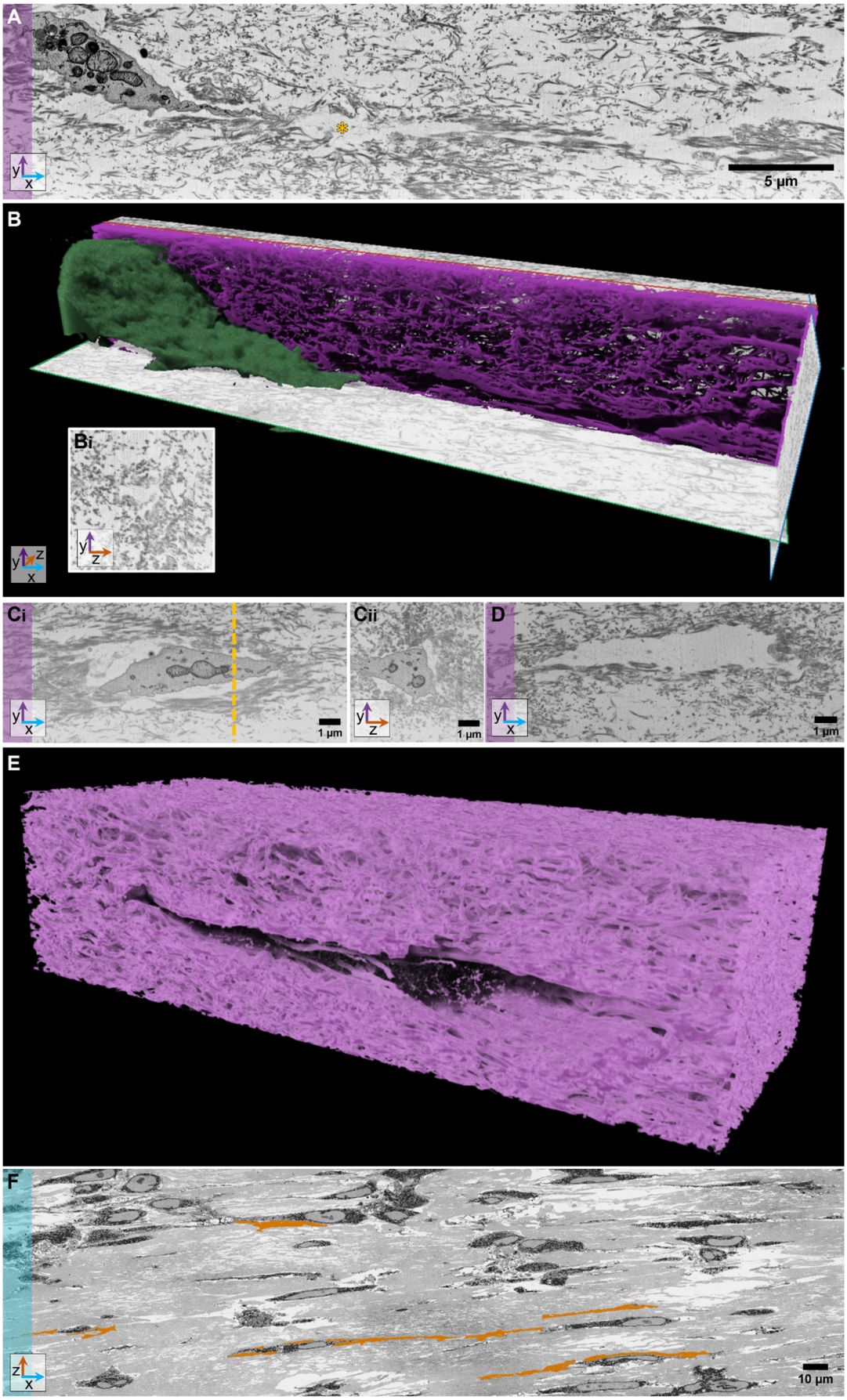
A
5 µm
B
Bi
Ci
1 µm
Cii
1 µm
D
1 µm
E
F
10 µm

Figure 4 - Tunnels and voids surrounded by collagen indicate active collagen organization by osteoblasts *A) FIB/SEM images along the longitudinal (XY) axis showed the presence of regions in the cell culture where the collagen aligned around a cell-free space extending from a cell protrusion (*). B) 3D reconstruction of the segmented cell (green) and collagen (magenta) in the 3D FIB/SEM stack showed that the cell-free space was shaped as a tunnel. Reslicing of the axial view (B_i) around the tunnel, showed that the tunnel was surrounded by collagen which showed a decreasing density at a larger distance from the center of the tunnel. C) FIB/SEM imaging (longitudinal, XY) showed that collagen in these cultures had a high density and alignment in close proximity to cells (C_i). The resliced axial view (C_{ii}, YZ, at dotted line) showed a gradient in collagen density around the cell. Scalebars: 1 µm. D) FIB/SEM imaging showed cell-free voids surrounded by dense and aligned collagen that showed a gradient when moving further away from the cell. Scalebar: 1 µm. E) 3D reconstruction of segmented collagen (magenta) surrounding a cell-shaped void region. F) AT-SEM imaging in the fibrin-rich core region showed the presence of voids (orange) next to cells in the mixed fibrin/collagen matrix. Scalebar: 10 µm.*

Discussion

In this study we developed a human MSC-based 3D cell culture using uniaxially fixed fibrin matrices, in which osteogenic differentiation, collagen matrix development, and the collagen-cell interface were studied. In accordance with previous reports (Iordachescu et al., 2018; Kim et al., 2021; Matsumoto et al., 2007; Sasaki et al., 2010; Sasaki et al., 2015), we observed that the uniaxial fixation of the culture induced alignment of the cells and the deposited collagen matrix solely through the activity of osteoblasts and osteocyte-like cells. Using a 3D multiscale imaging approach, combining 3D array tomography SEM, live fluorescence imaging, and 3D FIB/SEM (Figure 5), we were able to reveal structural details of the resulting culture that allow us to propose that the alignment of the newly deposited collagen matrix derives from the migration of the osteogenic cells as detailed below.

In addition to highly aligned layers of collagen that surround the embedded cells and follow their surface, collagen *tunnels* were observed in the bulk of the culture. In the latter, the collagen appears to have followed the shape of a cell or cellular protrusion, although these cellular structures were no longer observed. Here, the cell seems to have retracted after alignment or even to have completely moved out (Figure 4). The fact that well-defined tunnels are observed in the regions of high collagen density, while those in the fibrin-rich regions were much less well defined, suggests that the cross-linking of the collagen plays a role in the persistence of their shape after cells migrate away (Rodriguez-Pascual and Slatter, 2016). Similar stable collagen structures have been observed in studies using fibroblasts (Guidry and Grinnell, 1987) and fibrosarcoma cells (Fisher et al., 2009). However, their role and dynamics have not yet been elucidated.

Our data show that in our osteogenic culture, the density of the collagen was not a determining factor for fibril alignment, as both the high-density collagen in the peripheral region of the culture and the collagen in the lower-density bulk and core regions showed alignment. However, the collagen showed higher degrees of alignment in regions where cells are present than in the surrounding areas, suggesting that the osteoblasts play an active role in collagen organization.

Moreover, the observation of collagen with lower degrees of alignment closer to the fibrin-rich core of the culture as well as in between the dense cells in the peripheral layer, together with highly aligned collagen around cells (Figure 3, Figure 4 & Supplementary Figure A.2) leads us to hypothesize that during osteogenesis collagen is quickly deposited in a disorganized fashion, resembling the structures observed in woven bone (Weiner and Wagner, 1998), and that later longer cell-collagen interactions induce collagen alignment and organization. This phenomenon of cells actively re-arranging collagen after deposition has been previously observed in monolayer cultures of mouse osteoblasts (Lu et al., 2018) and in 3D cultures for other cell types, such as cancer cells (Kim et al., 2018; Miller et al., 2020; Pamonag et al., 2022). The re-arrangement of collagen by cancer cells is essential to mediate migration and thus invasion (Kim et al., 2018; Pamonag et al., 2022), while for the osteoblasts in our cultures, it is essential to develop the cell-cell interactions that are critical for osteogenic development (Kim and Adachi, 2019; Stains and Civitelli, 2005).

We observe a clearly distinguishable border between a cell-dense layer and a collagen-dense layer, even though at the start of the experiment, the cells were randomly and homogeneously distributed in the fibrin gel, indicating that the cells move through the deposited collagen during differentiation. The 3D reconstructions of the cells embedded in the dense collagen (Supplementary Figure A.3) suggest that the cells move towards the nutrient-rich periphery of the culture, while also the alignment of the collagen in lower-density areas points to the movement of the cells towards nutritional and oxygen gradients. The cell-matrix interactions during these movements will be associated with shear stress and traction forces (Lange and Fabry, 2013) and are likely the cause of the collagen organization. We propose that the high degree of alignment in the high-density collagen layers is caused by the repeated interaction with moving cells and the compacting of the packed fibrils by the dense, aligned cell layer.

Here, the interaction with osteoblasts leading to collagen alignment could be mediated by collagen binding integrins, such as integrin $\alpha_2\beta_1$ (Boraschi-Diaz et al., 2017; Kundu et al., 2009; Lee et al., 2020), of which the expression is increased during early osteogenic differentiation of hMSCs, followed by a decrease in later stages (Kundu et al., 2009). On the other hand, osteoblasts could potentially modulate their collagen-binding capacity by expressing non-integrin-dependent collagen-binding proteins, such as discoidin domain receptors (DDR) (Yang et al., 2020), which were shown to influence collagen patterning during bone development in early stage embryogenesis (Vogel et al., 1997).

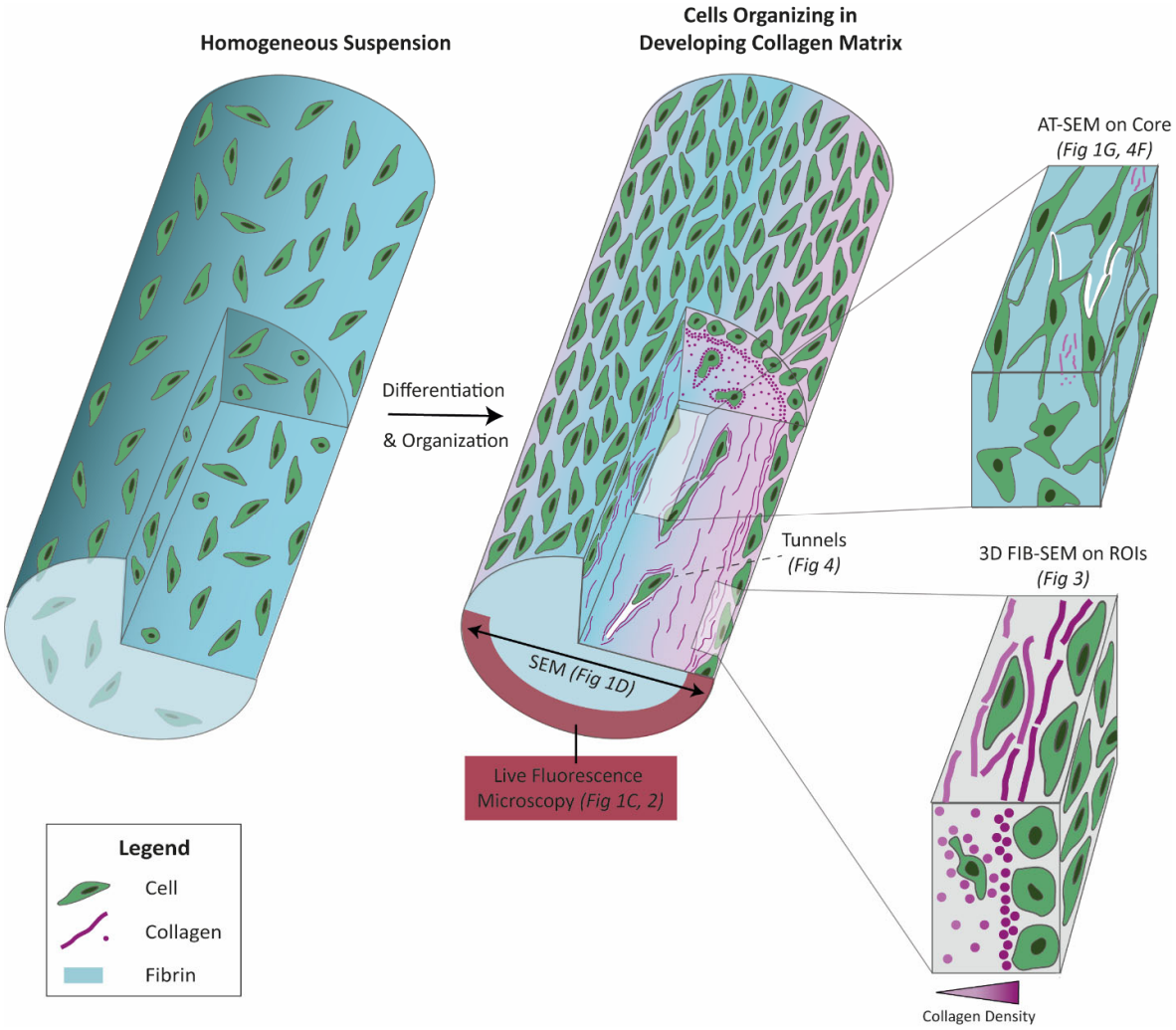

Figure 5 - Schematic representation of the development and multiscale analysis of our 3D osteogenic culture. *At the moment of seeding, cells are randomly distributed through the fibrin in a homogenous suspension. After gelation and differentiation, the cells have reorganized into a radial structure with a dense layer of aligned cells on*

319 *the periphery surrounding a dense layer of collagen, which can be observed by live fluorescence microscopy. SEM,*
320 *AT-SEM, and 3D FIB/SEM allowed for the reconstruction of the 3D environment of the periphery as well as the bulk*
321 *of the culture, showing that the collagen and cell density decrease towards the bulk of the culture, while the cells*
322 *present in this region are surrounded by denser collagen. This indicates that the cells migrate throughout the culture*
323 *towards the periphery, during which the collagen is contracted and organized.*

324 **Conclusion**

325 The 3D multiscale analysis of the developing uniaxially fixed human osteogenic cultures showed us variable levels of
326 cell and collagen alignment in different regions of the culture. We propose that in the early phase of osteogenesis,
327 the cells quickly deposit collagen with a low degree of organization Based on the fact that we start the culture from
328 a homogenous suspension of cells in fibrin and the final organization that we observed, we further propose that
329 during differentiation, osteoblasts move through the matrix towards the peripheral region of the culture, organizing
330 the collagen they come in contact with and leaving tunnels in the matrix after they have moved on. We observe that
331 tunnels in collagen-rich regions appear more shape-persistent than tunnels in fibrin-rich regions, most probably due
332 to stabilization by collagen cross-linking. Cell-dense layers show a high degree of collagen alignment, supporting the
333 active role of the cells that must impose shear forces on the matrix during their movement. With this, we show that
334 cell-matrix interactions play a crucial role in collagen alignment in early-stage osteogenesis, and that, in particular,
335 cellular motion can generate organized lamellar collagen matrices that subsequently can be mineralized.

336 In most vertebrates, including humans, the first matrix deposited during osteogenesis is disorganized woven bone
337 that is only after remodeling by the interplay of osteoblasts and osteoclasts converted into osteonal bone with
338 organized layers of mineralized lamellar collagen (Katsimbri, 2017; Weiner and Wagner, 1998). Indeed, we recently
339 showed that a human organoid grown under non-directional mechanical stimulation produced disorganized, woven
340 bone (Akiva et al., 2021). In contrast, fibrolamellar bone, the first deposited form of bone in many other, non-human,
341 vertebrates, already shows a high degree of parallel collagen alignment prior to remodeling (Magal et al., 2014;
342 Weiner and Wagner, 1998). Our experiments, and those of others (Iordachescu et al., 2018; Sasaki et al., 2010; Sasaki
343 et al., 2015), show that the alignment of collagen can also occur in the early stages of human osteogenesis and
344 hence is not genetically directed nor specific to species producing fibrolamellar bone. Instead, it can be induced by
345 applying longitudinal stress.

346 Our results thereby contribute to understanding the mechanistic aspects underlying collagen organization in
347 fibrolamellar bone, a topic that is under-investigated despite its importance for many species. Moreover, the ability
348 to organize collagen in 3D osteogenic cell cultures without osteoclastic remodeling may provide new routes for the
349 tissue engineering of load-bearing bone, as it has been notoriously difficult to achieve mechanically robust,
350 organized bone matrices through an interplay of osteoblasts and osteoclasts in *in vitro* cell cultures (de Wildt et al.,
351 2019).

352 **Materials and Methods**

353 Chemicals and cell culture supplements were bought from Sigma-Aldrich/Merck unless indicated differently. Cell
354 culture media and antibiotics were bought from Gibco.

355 ***Cell Culture***

356 Human mesenchymal stem cells (hMSCs) were isolated from bone marrow in University Medical Center Utrecht as
357 described previously (Pennings et al., 2019). In short, human bone plus marrow waste material from a 11-year old
358 female was obtained in accordance with the Declaration of Helsinki, with the approval of the Assessment Committee
359 Biobank (TCBio) of the University Medical Center Utrecht (Utrecht, The Netherlands) under the approved number
360 TCBio-18-685, and with the written consent of the parents. Bone marrow was diluted with an equal volume of
361 phosphate buffered saline (PBS) and filtered through a cell strainer (100µm). Mononuclear cells (MNC) were isolated
362 by centrifugation (320g, 20 min, RT) on a Ficoll-Paque gradient. The MNCs were washed with PBS to remove the
363 Ficoll and seeded at a density of 250.000 cells per cm^2 in MSC starting medium (αMEM (12571), 10% FCS, 100 U/mL
364 penicillin/100 µg/mL streptomycin (PenStrep, 15140122), 0.2mM ascorbic acid and 1 ng/mL recombinant human

365 FGF (R&D system, 233-GMP-025). The adherent cells were split by trypsinization at 80% confluency and frozen at
366 passage 2 (50% αMEM, 40% FCS, 10% DMSO) in a Mr. Frosty (overnight). After freezing, the vials were stored in LN_2.

367 hMSCs (passage 2 until passage 9) were cultured in a humidified incubator (37°C , 5% CO_2) in MSC proliferation
368 medium (PM; αMEM, 10% FCS, 100 U/mL-100 µg/mL PenStrep, 0.28 mM l-ascorbic acid-2-phosphate (AA2P
369 (49752)), 1 ng/mL recombinant human FGF. Upon 80% confluency, cells were split (1:10) by trypsinization (0.05%
370 Trypsin/0.53mM EDTA in PBS) according to standard cell culture protocols.

371 ***Aligned 3D culture supported by Velcro®***

372 The 3D cell cultures were grown in manually customized Ibidi µ-slide 8-wells slides (uncoated, 81501). The top edge
373 of the µ-slides was lowered with an electrical polisher, after which the wells were cleaned in ethanol (70%) in an
374 ultrasonic bath (5 min). Before use, the equipment and components were sterilized in 70% ethanol. Pieces of Velcro®
375 (~2x2mm, soft side) were attached to the edge of the wells with vacuum grease, while making sure that the hairs
376 were facing each other (Figure 1A). Then, polystyrene walls covered with a thin layer of vacuum grease on the edges
377 were placed on both sides of the Velcro® to create a closed cavity in the middle of the well in which the cell
378 suspension was sequentially seeded.

379 Stock solutions of bovine thrombin (605157, 50U/mL in αMEM, sterilized on a 0.2µm filter) and bovine fibrinogen
380 (60 mg/mL in αMEM, based on 77% clottable protein (F8630) were prepared in a laminar flow cabinet. Aliquots were
381 thawed on ice and thrombin was diluted in PM to a concentration of 5U/mL. Fibrinogen was diluted to a
382 concentration of 6 mg/mL in PM supplemented with amino-caproic acid (ACA, 2 mg/mL (A7824)).

383 Cells were trypsinized, counted, pelleted and resuspended in the diluted thrombin solution ($2x10^6$ cells/mL
384 thrombin). Next, the fibrinogen solution was mixed with an equal volume of cell suspension (final concentrations:
385 thrombin 2.5U/mL, fibrinogen 3 mg/mL, ACA 1 mg/mL, cells: $1x10^6$/mL) and 100 µL of the mix was pipetted between
386 the walls in each well, making sure that the suspension touched the Velcro®. The cells were polymerized (1h, 37°C,
387 5% CO_2) before the polystyrene walls were removed with help of a scalpel. Next, the cultures were grown for 2 days
388 in PM supplemented with ACA (1 mg/mL, 300 µL per well).

389 After 2 days, osteogenic differentiation was started by replacing PM with osteogenic induction medium (OIM; PM
390 supplemented with 10 mM β-Glycerophosphate (βGP, G9422) and 100 nM dexamethasone (D4902)). Medium was
391 refreshed three times a week. During the first 14 days of differentiation, the OIM was supplemented with ACA (1
392 mg/mL), while afterward, ACA was removed.

393 ***Calcium assay***

394 Cultures were harvested between 7 and 84 days of differentiation. The cultures were removed from the wells and
395 washed in PBS. Then, the culture was sliced into three pieces using a scalpel, and one part was incubated in HCl
396 (0.6M, 200µL) for 6 days (RT) to extract the mineral from the cultures, after which the samples were stored at -20°C
397 until use. For quantitative analysis of the calcium content, the samples were thawed on ice, and the supernatant
398 was used for an o-cresolphtalein colorimetric assay (Randox), according to the manufacturer's instructions. In short,
399 the reagents A and B were mixed in equal volumes and 250 µL was added to the samples (20 µL, pure or 10x diluted
400 in MQ). The reaction was incubated (15 min, RT) and the absorption was measured using a platereader (570 nm,
401 Biorad Benchmark Plus). Afterwards, the solid matrix was removed from the HCl and air-dried. The solids were
402 weighted to use for normalization of the calcium concentrations.

403 ***ALP activity assay***

404 To determine the ALP activity of the cell cultures, one third of each gel was stored in MQ (200 µL,
405 -20°C). The sample was lysed by 3 sequential freeze-thaw cycles and the solids were pelleted (1500g, 5 min). The
406 supernatant was used for an ALP activity assay, based on para-nitrophenyl phosphate (pNPP, S0942) conversion to
407 4-nitrophenol (241326). The cell lysates (50 µL diluted in 50 µL Alkaline Buffer Solution (0.5M, Sigma, A9226)) were
408 incubated with pNPP (100 µL, 5 mM in Alkaline Buffer) for 60 min at 37°C before the reaction was stopped by adding

409 NaOH (0.3M, 100 µL). Then, the fluorescence was determined using a Victor Fluorescence Platereader (405nm,
410 Biorad).

411 To normalize the activity, the samples were analyzed in a Bradford microplate assay (Biorad, 500-0006), according
412 to the manufacturer's protocol. In short, 10 µL of sample was mixed with 200 uL bradford reagent (diluted 1:5 with
413 demi-water) and the samples were incubated for 5 min (RT), before the absorption was measured using a
414 platereader (595 nm).

415 ***Fluorescence microscopy to monitor osteogenic differentiation***

416 3D cell cultures were fluorescently stained and imaged weekly during 5 to 7 weeks and at days 64 and 84 of
417 differentiation. The gels were incubated for at least 2h with CNA-OG488 (0.167µM in OIM, 488 nm, TU/e (Aper et
418 al., 2014)) in the incubator. Additionally, calcein blue (0.1 mg/mL, 405 nm (M1255)) and cell mask deep red (5 µg/mL,
419 630 nm (ThermoFisher, C10046)) were added to the staining medium for 2h. Next, the staining solution was
420 removed, and the gels were washed twice with PBS (5 min, 37°C), before fresh medium was added. Using an LSM900
421 upright (Carl Zeiss Microscopy GmbH, Germany), overview tile scans were made of the complete gel (objective: 5x
422 C Epiplan-APOCHROMAT/0.2 DIC M27, z-resolution=6.11µm, averaging=2, SR-4Y). Additionally, z-stacks were
423 recorded of one region of interest per gel (objective 10x C Epiplan-APOCHROMAT/0.4 DIC M27, z-resolution=1.48
424 µm, averaging=2, SR-4Y). After imaging, the medium was replaced, and the cells were placed back in the incubator.
425 For each experiment, the imaging settings were kept the same during the full duration of the experiment.

426 For live/dead staining Calcein-AM (500 nM) and propidium iodide (1 µg/mL) were diluted in OIM. The cells were
427 incubated for 30 min (37°C) with the staining medium and analyzed immediately after staining using a LSM900
428 upright microscope to record z-stacks with 5x and 10x objectives as described above.

429 ***Sample preparation for SEM***

430 At day 49, two gels were washed with PBS after fluorescent imaging and fixed in 2% glutaraldehyde (in 0.1M
431 Cacodylate buffer, pH = 7.4) for 90 min, while shaking (RT). After fixation, the gels were washed once quickly in
432 cacodylate buffer and sequentially washed twice for 30 min (shaking, RT). Next, the gels were embedded in 4% ultra-
433 low gelling temperature agarose (A5030, in MQ). The Ibidi slide was cooled on ice (30 min) to allow the agarose to
434 gel. Afterward, the agarose blocks containing the cell cultures were removed from the well and stored in cacodylate
435 buffer (4°C).

436 For post-fixation and staining, the samples were incubated in 2% OsO_4/1.5% $K_3Fe(CN)_6$/2 mM $CaCl_2$ in cacodylate
437 buffer (0.1M) for 30 min on ice, followed by an additional incubation at room temperature (30 min, shaking). Next,
438 the samples were washed in ddH_2O (5x 5 min each) and incubated in thiocarbohydrazide (0.5% in MilliQ, 30 min, RT,
439 shaking). The samples were washed in MilliQ (5x 5 min) and placed in 2% OsO_4 (in MilliQ, 30 min, RT, shaking). After
440 washing in MilliQ (5x 5 min), the samples were placed in 2% aqueous uranyl acetate (overnight, 4°C). Afterward, the
441 samples were washed in ddH_2O (5x 5 min) and stained in lead aspartate solution (pH 5.5) for 30 min (60°C). Next,
442 the samples were washed in ddH_2O (5x 5 min) and dehydrated on ice using an ascending ethanol series (50%, 70%,
443 90%, 3x 100% EtOH, 15 min per step, shaking) after which the samples were placed in acetone for 10 min (on ice).
444 Sequentially, the samples were embedded in Durcupan by step-wise increasing the concentration of Durcupan in
445 acetone to 100% Durcupan (25% 1.5h; 50% 1.5h; 75% overnight; 100%, twice 2.5h, 1.5h). The Durcupan was
446 polymerized at 60°C for 48h.

447 ***Sectioning for 3D Array Tomography SEM***

448 One of the embedded cultures was sectioned for array tomography SEM (AT-SEM). Ribbons of serial ultrathin
449 sections (400x200 µm, 80 nm thick, ~250 sections) were made using a Leica Artos 3D Ultramicrotome (Leica AT4
450 knife). The ribbons were placed on ITO glass and coated with 5 nm carbon (Leica ACE600) and overview images
451 (~170x480 µm) were made of all sections using a Zeiss Sigma 300 SEM (50 nm/pixel, Atlas 5), after which higher
452 resolution stacks were recorded (9 nm/pixel, 53x143 µm) from a selected region of interest.

Additionally, a section (200 nm thick) along the axial axis of the culture was prepared on ITO glass. The section was coated with 5nm carbon and an overview image was made using a Zeiss Sigma 300 SEM with Atlas 5 software (3kV, pixel size 15 nm), using the backscatter detector.

SEM and 3D FIB/SEM

One embedded culture was sectioned along the longitudinal axis on a microtome until the core of the culture was reached. An overview of the sample was imaged with a Zeiss Sigma 300 SEM (3kV, pixel size 35 nm) and regions of interest were recorded (3kV, pixel size 10 nm). The sample was then coated with a gold sputter coater (Edwards) and transferred to a Zeiss Crossbeam 550 FIB/SEM.

At the regions of interest, Pt and C were sequentially deposited before a coarse trench was milled using a 30 kV/30 nA FIB probe and smoothened with a 30 kV/1.5 nA FIB probe. Parameters for serial sectioning imaging were set in Atlas 3D software (Atlas Engine v5.3.3) to allow imaging at a 10x10x10 nm voxel size, using a 30 kV/700 pA probe for serial FIB milling. InLens secondary and backscattered (grid -876V) electron microscopy images were simultaneously recorded (line average n=1, dwell time 0.7x4 µs) using an acceleration voltage of 2.0 kV and a probe current of 500 pA. After imaging, the ESB and InLens data were exported from Atlas as a combined file, using a 0.25 ratio of Inlens/ESB.

Image analysis

Fluorescence images were analyzed in FIJI (version 1.52p). Using a macro (Supplementary Information B), maximum intensity projections (MIP) were made of the stitched tilescans (5x) and the brightness was adjusted for visualization purposes. For 10x images, a macro was used (Supplementary Information C) to prepare maximum intensity projections and perform orientation analysis with OrientationJ (σ=30 for cells; σ=12 for collagen, cubic spline) to extract color maps (OrientationJ Analysis (Püspöki et al., 2016)) as well as orientation histograms (OrientationJ Distribution (Rezakhaniha et al., 2012)). Orientation histograms were used in combination with the color maps to determine the quality of the analysis. In case no clear peak was present and the signal was too faint to determine reliable orientation color maps, the data were excluded from further analysis. The data from the orientation histograms (37 images from 4 experiments, containing data from 11 different gels) were then used to determine the peak maximum in Excel for the collagen as well as membrane orientation. The absolute difference between these values was used for analysis of the angles between the two components. To determine the full width at half maximum, the centers (35-145 degrees) of the histograms were transferred to Origin and fitted using a Lorentzian peak function.

3D Electron Microscopy Image Processing

AT-SEM data were aligned in Zeiss Atlas 5 and 210 sequential frames were exported. The frames were imported in Dragonfly ORS (Version 2022.2 for Windows, Comet Technologies Canada Inc. Montreal, Canada; software available at https://www.theobjects.com/dragonfly) and a U-NET++ network (U-NET++, Depth level: 5, Input Dimension: 3D) was trained for segmentation of cells in sequential steps, based on a total of 69 frames (~1% of total voxels annotated). Voids were annotated based on a selected range from the image histogram (255-255). The inner areas in the voids ROI were filled (3D) before the ROI was smoothened (kernel 9, 3D).

The 3D FIB/SEM stacks were first processed in FIJI to sequentially remove shadows (subtract background, rolling ball radius 500 pixels), optimize the histogram (math, subtract, value = 75) and optimize the contrast (Local Contrast Enhancement (CLAHE), block size = 49, slope = 1.5).

After this, the stacks were visualized and segmented in Dragonfly ORS (Version 2022.2). For segmentation, one of the stacks was imported in the Dragonfly ORS segmentation wizard and 36 frames (0.11% of total voxels annotated) were manually annotated for background, collagen and cells (13% cells, 35.3% collagen, 51,7% background). A pre-trained Dragonfly neural network (YOLOv3, U-NET, Depth level: 5, Input Dimension: 2D, pre-trained on ORS500Kv01) was trained using these segmentations in 5 sequential steps, using increasing numbers of frames (from 5 to 36). To apply the model on the other full stacks, the initial trained model was optimized for the specific stack by importing

498 the model in the Segmentation Wizard with the new stack and re-training on 5 (R16) or 8 (R13) manually assigned
499 frames (R13: 0.15%/R16: 0.03% of total voxels annotated). For segmentation of cropped regions from all stacks, the
500 initial model was used for segmentation using 2D or 3D (major vote) segmentation mode, while adjusting the
501 brightness/contrast settings to correct for differences between the stacks. After segmentation, manual corrections
502 and Boolean operations (e.g. fill holes) were applied to optimize the annotations. Next, the collagen was exported
503 as ROI and used for orientation analysis in FIJI (OrientationJ, σ=3, cubic spline). For density measurement, ROIs of
504 comparable sizes were selected that contained only collagen and the percentage of labeled voxels was copied from
505 the Dragonfly characteristics.

506 **Acknowledgements**

507 The authors thank Harrie Weinans and Ralph Sakkers from University Medical Center Utrecht for providing the
508 hMSCs. The project was supported by an European Research Council (ERC) Advanced Investigator grant (H2020-ERC-
509 2017-ADV-788982-COLMIN) to N.S. A.A. was also supported by a VENI grant from the Netherlands Scientific
510 Organization NWO (VI.Veni.192.094).

511 **References**

512 Akiva, A., Melke, J., Ansari, S., Liv, N., Meijden, R., Erp, M., Zhao, F., Stout, M., Nijhuis, W.H., Heus, C., Muñiz
513 Ortera, C., Fermie, J., Klumperman, J., Ito, K., Sommerdijk, N., Hofmann, S., 2021. An Organoid for Woven
514 Bone. Adv Funct Mater 31, 2010524.
515 Aper, S.J., van Spreeuwel, A.C., van Turnhout, M.C., van der Linden, A.J., Pieters, P.A., van der Zon, N.L., de la
516 Rambelje, S.L., Bouten, C.V., Merkx, M., 2014. Colorful protein-based fluorescent probes for collagen
517 imaging. PLoS One 9, e114983.
518 Blair, H.C., Larrouture, Q.C., Li, Y., Lin, H., Beer-Stoltz, D., Liu, L., Tuan, R.S., Robinson, L.J., Schlesinger, P.H., Nelson,
519 D.J., 2017. Osteoblast Differentiation and Bone Matrix Formation In Vivo and In Vitro. Tissue Eng Part B
520 Rev 23, 268-280.
521 Boraschi-Diaz, I., Wang, J., Mort, J.S., Komarova, S.V., 2017. Collagen Type I as a Ligand for Receptor-Mediated
522 Signaling. Frontiers in Physics 5.
523 Budyn, E., Gaci, N., Sanders, S., Bensidhoum, M., Schmidt, E., Cinquin, B., Tauc, P., Petite, H., 2018. Human Stem
524 Cell Derived Osteocytes in Bone-on-Chip. MRS Advances 3, 1443-1455.
525 Buss, D.J., Kröger, R., McKee, M.D., Reznikov, N., 2022. Hierarchical organization of bone in three dimensions: A
526 twist of twists. Journal of Structural Biology: X 6, 100057.
527 de Jonge, N., Kanters, F.M., Baaijens, F.P., Bouten, C.V., 2013. Strain-induced collagen organization at the micro-
528 level in fibrin-based engineered tissue constructs. Ann Biomed Eng 41, 763-774.
529 de Wildt, B.W.M., Ansari, S., Sommerdijk, N.A.J.M., Ito, K., Akiva, A., Hofmann, S., 2019. From bone regeneration to
530 three-dimensional in vitro models: tissue engineering of organized bone extracellular matrix. Current
531 Opinion in Biomedical Engineering 10, 107-115.
532 Fisher, K.E., Sacharidou, A., Stratman, A.N., Mayo, A.M., Fisher, S.B., Mahan, R.D., Davis, M.J., Davis, G.E., 2009.
533 MT1-MMP- and Cdc42-dependent signaling co-regulate cell invasion and tunnel formation in 3D collagen
534 matrices. J Cell Sci 122, 4558–4569.
535 Fratzl, P., Weinkamer, R., 2007. Nature's hierarchical materials. Progress in Materials Science 52, 1263-1334.
536 Golub, E.E., Boesze-Battaglia, K., 2007. The role of alkaline phosphatase in mineralization. Current Opinion in
537 Orthopaedics 18, 444-448.
538 Guidry, C., Grinnell, F., 1987. Contraction of Hydrated Collagen Gels by Fibroblasts: Evidence for Two Mechanisms
539 by which Collagen Fibrils are Stabilized. Collagen and Related Research 6, 515-529.
540 Husch, J.F.A., Coquelin, L., Chevallier, N., Tiemessen, D., Oosterwijk, E., van Rheden, R., Woud, C., Vossen, J.,
541 Leeuwenburgh, S.C.G., van den Beucken, J.J.J.P., 2023. Comparison of Osteogenic Capacity and
542 Osteoinduction of Adipose Tissue-Derived Cell Populations. Tissue Eng Part C Methods 29, 216-227.
543 Iordachescu, A., Amin, H.D., Rankin, S.M., Williams, R.L., Yapp, C., Bannerman, A., Pacureanu, A., Addison, O.,
544 Hulley, P.A., Grover, L.M., 2018. An In Vitro Model for the Development of Mature Bone Containing an
545 Osteocyte Network. Adv Biosyst 2, 1700156.
546 Jaiswal, N., Haynesworth, S.E., Caplan, A.I., Bruder, S.P., 1998. Osteogenic differentiation of purified, culture-
547 expanded human mesenchymal stem cells in vitro. Journal of Cellular Biochemistry 64, 295-312.
548 Kassem, M., Rungby, J., Mosekilde, L., Eriksen, E.F., 1992. Ultrastructure of human osteoblasts and associated
549 matrix in culture. APMIS 100, 490-497.
550 Katsimbri, P., 2017. The biology of normal bone remodelling. Eur J Cancer Care (Engl) 26.

551 Kim, D.-H., Ewald, A.J., Park, J., Kshitiz, Kwak, M., Gray, R.S., Su, C.-Y., Seo, J., An, S.S., Levchenko, A., 2018.
552 Biomechanical interplay between anisotropic re-organization of cells and the surrounding matrix
553 underlies transition to invasive cancer spread. Scientific Reports 8, 14210.
554 Kim, J., Adachi, T., 2019. Cell Condensation Triggers the Differentiation of Osteoblast Precursor Cells to Osteocyte-
555 Like Cells. Front. Bioeng. Biotech. 7.
556 Kim, J., Ishikawa, K., Sunaga, J., Adachi, T., 2021. Uniaxially fixed mechanical boundary condition elicits cellular
557 alignment in collagen matrix with induction of osteogenesis. Scientific Reports 11, 9009.
558 Kundu, A.K., Khatiwala, C.B., Putnam, A.J., 2009. Extracellular matrix remodeling, integrin expression, and
559 downstream signaling pathways influence the osteogenic differentiation of mesenchymal stem cells on
560 poly(lactide-co-glycolide) substrates. Tissue Eng Part A 15, 273-283.
561 Lange, J.R., Fabry, B., 2013. Cell and tissue mechanics in cell migration. Experimental Cell Research 319, 2418-2423.
562 Lee, H.M., Seo, S.-R., Kim, J., Kim, M.K., Seo, H., Kim, K.S., Jang, Y.-J., Ryu, C.J., 2020. Expression dynamics of
563 integrin α2, α3, and αV upon osteogenic differentiation of human mesenchymal stem cells. Stem Cell
564 Research & Therapy 11, 210.
565 Lu, P., Lu, Y., 2021. Born to Run? Diverse Modes of Epithelial Migration. Front. Cell. Dev. Biol. 9, 704939.
566 Lu, Y., Kamel-El Sayed, S.A., Wang, K., Tiede-Lewis, L.M., Grillo, M.A., Veno, P.A., Dusevich, V., Phillips, C.L.,
567 Bonewald, L.F., Dallas, S.L., 2018. Live Imaging of Type I Collagen Assembly Dynamics in Osteoblasts Stably
568 Expressing GFP and mCherry-Tagged Collagen Constructs. J Bone Miner Res 33, 1166-1182.
569 Magal, R.A., Reznikov, N., Shahar, R., Weiner, S., 2014. Three-dimensional structure of minipig fibrolamellar bone:
570 Adaptation to axial loading. Journal of Structural Biology 186, 253-264.
571 Matsumoto, T., Sasaki, J., Alsberg, E., Egusa, H., Yatani, H., Sohmura, T., 2007. Three-dimensional cell and tissue
572 patterning in a strained fibrin gel system. PLoS One 2, e1211.
573 Meesuk, L., Suwanprateeb, J., Thammarakcharoen, F., Tantrawatpan, C., Kheolamai, P., Palang, I.,
574 Tantikanlayaporn, D., Manochantr, S., 2022. Osteogenic differentiation and proliferation potentials of
575 human bone marrow and umbilical cord-derived mesenchymal stem cells on the 3D-printed
576 hydroxyapatite scaffolds. Sci Rep 12, 19509.
577 Miller, A.E., Hu, P., Barker, T.H., 2020. Feeling Things Out: Bidirectional Signaling of the Cell–ECM Interface,
578 Implications in the Mechanobiology of Cell Spreading, Migration, Proliferation, and Differentiation. Adv
579 Healthc Mater 9, 1901445.
580 Miron, R.J., Zhang, Y.F., 2012. Osteoinduction: A Review of Old Concepts with New Standards. Journal of Dental
581 Research 91, 736-744.
582 Nasello, G., Alaman-Diez, P., Schiavi, J., Perez, M.A., McNamara, L., Garcia-Aznar, J.M., 2020. Primary Human
583 Osteoblasts Cultured in a 3D Microenvironment Create a Unique Representative Model of Their
584 Differentiation Into Osteocytes. Front Bioeng Biotechnol 8, 336.
585 Pamonag, M., Hinson, A., Burton, E.J., Jafari, N., Sales, D., Babcock, S., Basha, R., Hu, X., Kubow, K.E., 2022.
586 Individual cells generate their own self-reinforcing contact guidance cues through local matrix fiber
587 remodeling. PLoS One 17, e0265403.
588 Pennings, I., van Dijk, L.A., van Huuksloot, J., Fledderus, J.O., Schepers, K., Braat, A.K., Hsiao, E.C., Barruet, E.,
589 Morales, B.M., Verhaar, M.C., Rosenberg, A.J.W.P., Gawlitta, D., 2019. Effect of donor variation on
590 osteogenesis and vasculogenesis in hydrogel cocultures. Tissue Engineering and Regenerative Medicine
591 13, 433-445.
592 Püspöki, Z., Storath, M., Sage, D., Unser, M., 2016. Transforms and Operators for Directional Bioimage Analysis: A
593 Survey. Adv. Anat. Embryol. Cell Biol. 219, 69-93.
594 Rezakhaniha, R., Agianniotis, A., Schrauwen, J.T.C., Griffa, A., Sage, D., Bouten, C.V.C., van de Vosse, F.N., Unser,
595 M., Stergiopulos, N., 2012. Experimental investigation of collagen waviness and orientation in the arterial
596 adventitia using confocal laser scanning microscopy. Biomechanics and Modeling in Mechanobiology 11,
597 461-473.
598 Reznikov, N., Shahar, R., Weiner, S., 2014. Bone hierarchical structure in three dimensions. Acta Biomater 10,
599 3815-3826.
600 Rodriguez-Pascual, F., Slatter, D.A., 2016. Collagen cross-linking: insights on the evolution of metazoan
601 extracellular matrix. Scientific Reports 6, 37374.
602 Sasaki, J.-I., Matsumoto, T., Egusa, H., Nakano, T., Ishimoto, T., Sohmura, T., Yatani, H., 2010. In vitro engineering
603 of transitional tissue by patterning and functional control of cells in fibrin gel. Soft Matter 6.
604 Sasaki, J., Matsumoto, T., Imazato, S., 2015. Oriented bone formation using biomimetic fibrin hydrogels with three-
605 dimensional patterned bone matrices. Journal of Biomedical Materials Research Part A 103, 622-627.
606 Stains, J.P., Civitelli, R., 2005. Cell-cell interactions in regulating osteogenesis and osteoblast function. Birth Defects
607 Research Part C: Embryo Today: Reviews 75, 72-80.

608 Tenenbaum, H.C., 1981. Role of Organic Phosphate in Mineralization of Bone in vitro. Journal of Dental Research
609 60, 1586-1589.
610 Tenenbaum, H.C., Heersche, J.N.M., 1982. Differentiation of osteoblasts and formation of mineralized bone in
611 vitro. Calcified Tissue International 34, 76-79.
612 Thrivikraman, G., Athirasala, A., Gordon, R., Zhang, L., Bergan, R., Keene, D.R., Jones, J.M., Xie, H., Chen, Z., Tao, J.,
613 Wingender, B., Gower, L., Ferracane, J.L., Bertassoni, L.E., 2019. Rapid fabrication of vascularized and
614 innervated cell-laden bone models with biomimetic intrafibrillar collagen mineralization. Nat Commun
615 10, 3520.
616 Vogel, W., Gish, G.D., Alves, F., Pawson, T., 1997. The Discoidin Domain Receptor Tyrosine Kinases Are Activated by
617 Collagen. Molecular Cell 1, 13-23.
618 Weiner, S., Wagner, H.D., 1998. THE MATERIAL BONE: Structure-Mechanical Function Relations. Annu Rev Mater
619 Sci 28, 271-298.
620 Westhauser, F., Karadjian, M., Essers, C., Senger, A.-S., Hagmann, S., Schmidmaier, G., Moghaddam, A., 2019.
621 Osteogenic differentiation of mesenchymal stem cells is enhanced in a 45S5-supplemented β-TCP
622 composite scaffold: an in-vitro comparison of Vitoss and Vitoss BA. PLoS One 14, e0212799.
623 Yang, H., Sun, L., Cai, W., Gu, J., Xu, D., Deb, A., Duan, J., 2020. DDR2, a discoidin domain receptor, is a marker of
624 periosteal osteoblast and osteoblast progenitors. Journal of Bone and Mineral Metabolism 38, 670-677.
625 Zernik, J., Twarog, K., Upholt, W.B., 1990. Regulation of alkaline phosphatase and alpha2(I) procollagen synthesis
626 during early intramembranous bone formation in the rat mandible. Differentiation 44, 207-215.